Journal of the Meteorological Society of Japan, Vol. 88, No. 3, pp. 409–424, 2010.
DOI:10.2151/jmsj.2010-309

Multistatic Radar Observation of a Fine-Scale Wind Field with a Coupling-Compensated Adaptive Array Technique

Koji NISHIMURA

Research Organization of Information and Systems, Tokyo, Japan

Tomoyuki HARADA and Toru SATO

Kyoto University, Kyoto, Japan

(Manuscript received 10 December 2008, in final form 02 March 2010)

Abstract

As part of the Coupling Processes in the Equatorial Atmosphere (CPEA-II) Campaign, multistatic radar observations of local wind field were conducted using the Equatorial Atmosphere Radar and two auxiliary receiver arrays in West Sumatra, Indonesia, in December 2005. For obtaining velocity estimates from atmospheric echoes received by the two small arrays that have a high sidelobe level due to their small effective aperture, an adaptive clutter rejection process is required. Because of the existence of electromagnetic coupling between antennas and the ground, the relative phase, in terms of an echo received by separate antennas, cannot be accurately predicted only with given positions of antennas and the target volume. The phase error leads to degradation of desired atmospheric echoes in the output of the adaptive clutter rejection process. In order to compensate for the mutual coupling effect, we proposed a method to estimate the phase error corresponding to several directions in which atmospheric echoes were observed with particularly high signal-to-noise ratio (SNR). The estimates were interpolated at every necessary directional point using linear fit, thereby resulting in a successful removal of ground clutters without a serious loss of SNR. With this method, we have obtained a partial data set of the wind field. The wind field in the lower troposphere shows small-scale fluctuations on a horizontal scale of $\sim$500 m. We also present an attempt to interpret the fluctuation in a composite of multiple plane waves, employing a non-orthogonal decomposition method using a generalized inverse.

1. Introduction

The equatorial region, where absorption of solar radiation is maximal, is the largest source of heat energy in the earth's atmosphere. In particular, the Indonesian islands, where the water and lands are characteristically intertwined, are thought to be one of the largest sources of heat and water vapor. Various physical processes in the atmosphere are coupled with one another from the boundary layer to the thermosphere and have a global influence. Coupling Processes in the Equatorial Atmosphere (CPEA) research projects were conducted from 2001 to 2007 to investigate the mechanism and influence of these coupling processes (Fukao 2006).

As part of the CPEA research projects, we investigate small-scale dynamics of the troposphere using the Equatorial Atmosphere Radar (EAR). The resolution of an atmospheric radar can be improved using auxiliary equipment by two different approaches. Multiple-Doppler radar is one of the techniques that can determine multidimensional wind vectors at each point of interest by simultaneous observations using multiple radars. Ray et al.

Corresponding author: Koji Nishimura, Transdisciplinary Research Integration Center, Research Organization of Information and Systems, Tokyo 174-8515, Japan. (c/o National Institute of Polar Research).
E-mail: knish@nipr.ac.jp

(1975) observed the structure of a tornadic storm using an S-band dual-Doppler weather radar. Gal-Chen and Kropfli (1984) examined thermodynamic parameters using an X-band dual-Doppler radar and a theoretical model of the boundary layer. The other technique is multistatic radar, which employs one conventional transmitting radar and multiple non-transmitting radar receivers to collect multiple Doppler velocity data in obliquely scattered radio waves. Wurman et al. (1993) have developed a low-cost bistatic S-band multiple-Doppler radar network to study the dynamics in precipitating clouds. Regarding the large MST radar, for which an ad-hoc dual or multiple radar equipment is not feasible, this technique is the only solution to realize multidimensional Doppler observations. Therefore, we developed a multistatic system consisting of two small digital receiver arrays based on the EAR.

Regarding atmospheric radars, persistent ground clutters must be considered because of their ability to affect the estimation of small Doppler velocity component of the wind. In the monostatic Doppler spectrum of EAR, only one spiky clutter appears at $f = 0$ and a flared skirt around it due to propagation-induced fading does not largely appear above the noise floor. Therefore, the clutter can be effectively removed only by eliminating the DC component. However, in our low-gain multistatic receiver arrays, which have sidelobes about 15 dB higher than those of EAR, the clutter is largely enhanced and its skirt appears above the noise floor. Therefore, they cannot be removed easily by temporal or spectral filtering.

To address this problem, we introduced adaptive array processing techniques by taking advantage of a highly flexible digital receiver system. These techniques are based on the principle that undesired signals in the output of an array can be eliminated by optimizing the weight of each element to minimize the average output power, with a condition that it holds a non-zero response to the desired direction. This principle is known as the Directional Constraint Minimum Power (DCMP) or Minimum Variance Distortionless Response (MVDR) (Takao et al. 1976).

To aim the beam to a desired direction, the three-dimensional positions of all the antennas must be known. However, DCMP is quite sensitive to position errors relative to antennas and target direction, suppressing of desired signals. To relieve this sensitivity, some variations have been proposed. Cox et al. (1987) proposed the application of an inequality norm constraint (NC) on the weight vector to stabilize the reaction of the main lobe. This algorithm takes advantage of the characteristic reaction of the weight amplitude, which becomes large in the case of a phase error, to move the signal from a slightly off-pointed direction while satisfying the directional constraint (Hudson 1981). We used the NC method, which was used for atmospheric observation with the MU radar basis (Kamio et al. 2004). Another principle was suggested by Stoica et al. (2003), which applies an NC on the difference between the outcoming weight vector and the given steering vector (Robust Capon Beamformer (RCB) method). It has been reported that the RCB method is stable against the same kinds of errors as is the NC method (Wang et al. 2003; Ward et al. 2003).

Despite their effectiveness, it has become clear that the algorithms are not yet stable with regard to configuration of the arrays and reject desired echoes. This might be because of the existence of electromagnetic effects such as mutual coupling, hiding, and the ground effect. These effects, which are not significant in conventional non-adaptive phased array applications, may cause discrepancies between the phases of received echoes and those expected from the geometrical configuration.

Phase errors are usually not very large and, from a practical point of view, are even more difficult and ineffective to deduce from given individual antenna structure, three-dimensional position, inclination, and condition of the base soil. If the desired echo can be discriminated, one possible approach is to apply the NC-DCMP under the condition that the power of the desired echo is maintained constant. This approach is applicable only to very bright echoes that can be discriminated in the spectral region. However, only a few such bright echoes are recognized in an entire set of atmospheric echoes observed between ground level and high altitude. Therefore, it is assumed that phase errors due to electromagnetic effects do not drastically change and can be estimated using a smooth function.

With this method, phase biases are estimated from an observed atmospheric echo without the need for additional physical measurements. This systematic combination of mutual coupling compensation and adaptive array processing has not been reported previously. In this paper, the procedure and some observation results are introduced. First, the principle of a multistatic radar and the system configuration are briefly reviewed.

2. Observation system and observation scheme

Multistatic observations were performed for about 400 hours, from December 5 to 21, 2005, as part of the CPEA-II campaign. The observation system was built based on the EAR (47 MHz, 5 kW average) (Yamamoto et al. 2003) in West Sumatra, Indonesia, which is a conventional high-gain monostatic atmospheric radar. To make it multistatic, two auxiliary receiver arrays consisting of a dozen antennas each (Nishimura et al. 2006) were used. Each antenna was connected to its own PC-based digital receiver with fully adaptive capabilities. Major specifications of the receiver hardware are as follows. Antenna: 4-element Yagi; Pre-amplifier: gain = 25 dB, NF < 2 dB; AD Converter: resolution = 14 bits, sampling rate = 64 MHz. Signals received at this rate were down-converted to 2 MHz on the receiver board and stored in the PC memory. Pulse compression and coherent synthesis processes were performed for the stored signals to de-modulate the optimally modulated codes. The arrays were set ~1100 m west (Site A) and ~1300 m south (Site B) of the EAR. A plan view of the sites is shown in Fig. 1. Site A contained 12 Yagi and 2 vertical dipole antennas, and Site B contained 13 Yagi and 3 vertical dipole antennas (data from these dipoles are not used in the analysis hereafter). The positions of the antennas are listed in Table 1 and depicted in Figs. 2, 3 to intuitively show the condition of the base

Table 1. Three-dimensional position of antennas at each receiver site.

	Site A		
No.	X(m)	Y(m)	Z(m)
1	5.27	−11.30	2.65
2	8.12	−7.84	2.22
3	3.78	−7.11	1.71
4	4.77	−15.59	3.44
5	1.14	−12.99	2.45
6	−0.30	−8.62	1.87
7	0.23	−4.44	0.87
8	4.47	−2.79	1.31
9	8.82	−3.56	0.80
10	12.27	−6.52	0.22
11	11.65	−10.87	1.43
12	8.94	−14.31	2.57

	Site B		
No.	X(m)	Y(m)	Z(m)
1	3.20	−9.29	0.77
2	3.39	−4.84	0.74
3	7.12	−7.12	0.70
4	0.66	−12.68	0.86
5	−1.25	−8.92	0.79
6	−0.93	−4.36	0.71
7	1.30	−0.78	0.74
8	5.54	−0.98	0.70
9	9.65	−3.51	0.71
10	11.57	−7.51	0.74
11	9.22	−11.39	0.80
12	5.11	−13.31	0.75
13	−4.05	−12.46	0.81

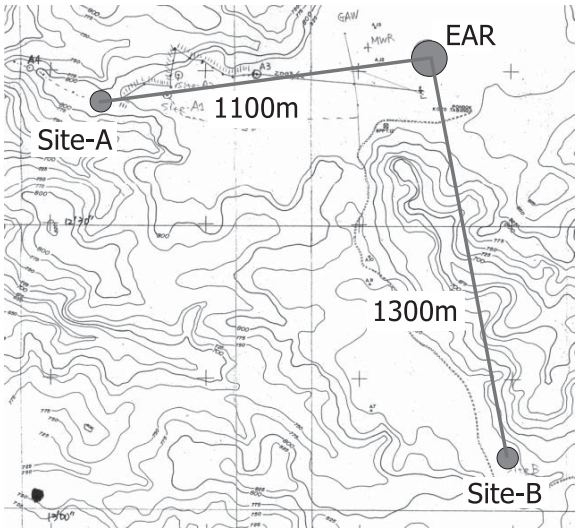

Fig. 1. A plan view of the EAR and two receiver sites.

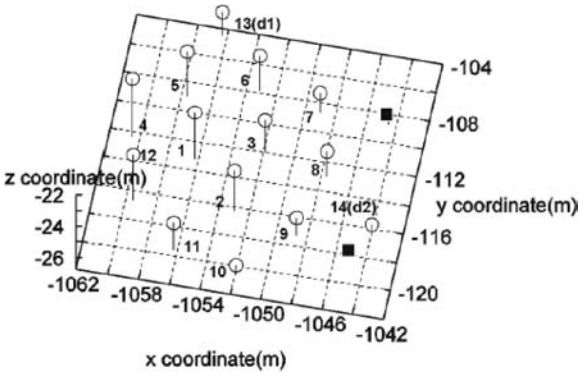

Fig. 2. Position of antennas at Site A exhibiting the uneven ground base with a height difference of 3 m.

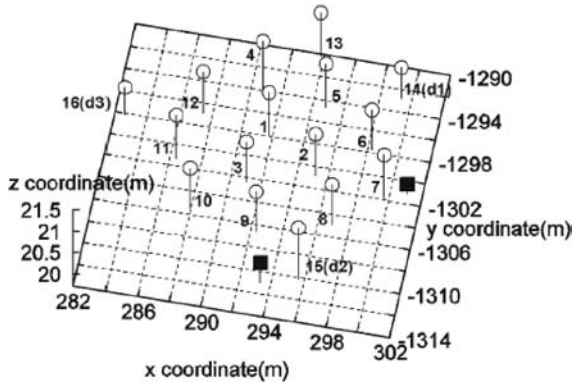

Fig. 3. Position of antennas at Site B.

Table 2. Major parameters of the transmission modes of the EAR.

Mode	A	B	C
Inter-pulse Period (μs)	400	400	200
Subpulse Length (μs)	1	1	1
Code Length	32	32	16
No. of Coherent Integrations	32	32	16
No. of Beams	6	8	5
Period (s)	78.64	65.54	40.96

ground. Note that the height of each antenna from the ground was set as a constant.

Three transmission modes of EAR were alternated about every 1 min. For all transmission modes, the Spano and Ghebrebrhan Code (Spano and Ghebrebrhan 1996), which is optimally designed for MST radar observations, was used for pulse compression. The main parameters of the transmission modes are listed in Table 2. Among the modes listed, Mode C was not used for this multistatic observation because it is devoted particularly to radio-acoustic sounding system (RASS) observations, and its frequency is shifted to match the speed of sound. The order and directions of the beam in Modes A and B are shown in Table 3.

3. Calibration of the intrinsic phase of receivers

Each receiver has its own intrinsic phase that must be calibrated before array processing of received signals. This intrinsic phase is partly due to the individual characteristics of analog parts such as RF cables, filters, and amplifiers. These components can be regarded as constant throughout the observations. The intrinsic phase is also partly due to the difference in integration timing in the down-conversion process from 64 MS/s to 2 MS/s, which is not synchronized among all digital receivers in each array even though the master clock of 64 MHz is synchronized. Since this component does not change while the receivers are powered on, the phase calibration process is performed only once after every rebooting of the receiver systems. Calibration is performed as follows. At the i^{th} receiver, the phase of an observed atmospheric echo from a point indexed by j is related to the receiver's position $\boldsymbol{r}_i$ and the intrinsic phase φ given by

$$\psi_{ij} = \vartheta_j(t) + \boldsymbol{k}_j \cdot (\boldsymbol{r}_i - \boldsymbol{r}_0) + \varphi_i \quad (1 \le i \le N,\ 1 \le j \le M) \tag{1}$$

where $\psi_j(t)$ is the phase of an atmospheric echo as a function of time, $\boldsymbol{r}_0$ is an arbitrary constant reference vector commonly given to all receivers within an array, and $\boldsymbol{k}_j$ is the wavenumber vector. Since an operation replacing the two unknowns $\vartheta_j(t)$ and φ_i with $\vartheta_j(t) + \alpha$ and $\varphi_i - \alpha$, respectively, where α is an arbitrary value, does not change the measurements ψ_{ij}, it is impossible to determine all the unknowns in (1). However, what we need to know is relative value of φ among receivers. Using the first ($i = 1$) receiver as a reference, we obtain

$$\psi'_{ij} = \boldsymbol{k}_j \cdot (\boldsymbol{r}_i - \boldsymbol{r}_1) + \varphi'_i (2 \le i \le N,\ 1 \le j \le M) \tag{2}$$

where the primes ($'$) show differences from the reference, e.g., $\psi'_{ij} = \psi_{ij} - \psi_{1j}$ and $\varphi'_i = \varphi_i - \varphi_1$. φ'_i ($2 \le i \le N$) is immediately obtained from (2).

This is sufficient for calibrating the phases as long as mutual coupling of antennas can be ignored. However, in real data, this method does not work well for adaptive array processing, which requires more accurate phase calibration than conventional beam forming techniques, as shown below.

Table 3. Direction of the beams in Modes A and B.

	(zenith angle, azimuth)	
No.	Mode A	Mode B
1	(0.0, 0.0)	(0.0, 0.0)
2	(10.0, 0.0)	(20.0, 135.0)
3	(10.0, 90.0)	(20.0, 225.0)
4	(0.0, 0.0)	(20.0, 315.0)
5	(10.0, 180.0)	(30.0, 180.0)
6	(10.0, 270.0)	(30.0, 210.1)
7		(30.0, 240.1)
8		(30.0, 270.0)

4. Post-set beam-steering and adaptive clutter rejection

To accurately estimate the Doppler velocity of each target volume, the echo signals received by multiple antennas within a receiver array need to be added. Since the received signals are stored separately on each receiver in our system, coherent addition of signals can be done offline. In a bistatic receiver configuration, where the path of the transmitted radio pulse does not match the line-of-sight direction from a receiver, the reception beams must be adjusted sample-by-sample to point at a target volume traveling at the speed of light.

Receivers are synchronized offline by detecting direct waves from EAR before every 3-min observation cycle. Once the receivers are synchronized, the reception beam can point at a target by adjusting the relative phases. The relative phase of an antenna for a target direction described by the wavenumber vector $\boldsymbol{k}$ is given by (1).

Figure 4 shows a resulting Doppler spectrum of a signal obtained from the coherent addition of 10 antennas at Site A. The bright curve reaching to a height of about 5 km corresponds to the wind velocity at each height. Here one can see strong ground clutters at zero velocity. The widely spread signal across the bottom of the figure is a mixture of the skirt of ground clutters and transmission noise of the EAR, which is directly received and not cancelled in the pulse compression procedure. Note that the contour is truncated around the peak of ground clutters in this figure.

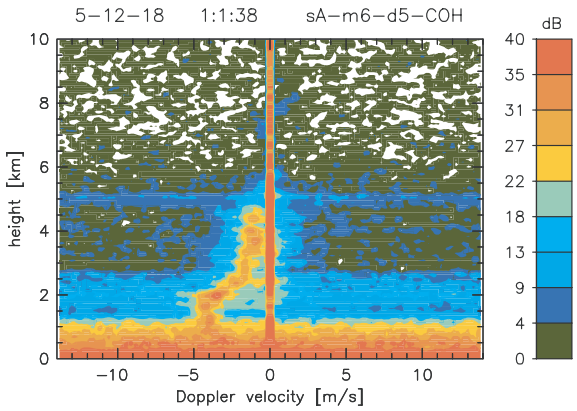

Fig. 4. Doppler spectrum observed at Site A with only post-set beam-steering. The intense stripe from the bottom to top at zero velocity indicates ground clutters, while the curved band to a height of 5 km is the atmospheric echo.

In addition to beam-steering, ground clutters must be simultaneously rejected in our system. This is because the receiver arrays consisting of a dozen antennas have very small effective areas with diameters of approximately 3λ. Moreover, have quite large sidelobe responses compared to EAR that does not have such a mechanism. The algorithm we employed to reject ground clutter is the NC DCMP (Kamio et al. 2004). This algorithm is derived from the following principle: the average output power is minimized by controlling the weight vector, within a particular norm bound, on the condition that the spatial response to a specific direction of interest is constant. This principle is written as

$$\text{minimize} \quad \left(P_{\text{out}} = \frac{1}{2} \boldsymbol{w}^{\text{H}} R \boldsymbol{w} \right)$$

$$\text{subject to} \quad \boldsymbol{w}^{\text{H}} \boldsymbol{c} = 1 \text{ and } \boldsymbol{w}^{\text{H}} \boldsymbol{w} < 1 + \delta$$

where $\boldsymbol{w}$ is the weight vector, $\boldsymbol{c}$ is a steering vector defining the directional constraint, R is a correlation matrix of the input signals, and δ is the allowance for the weight vector. If δ is too small, the clutters cannot be removed effectively. However, if δ is large enough to change the shape of the main lobe, the total noise output increases and the desired echo signals are suppressed. Therefore, δ has to be set to a value that is small enough to cancel clutters. With empirical means, we set this value to 0.5. The solution is given by appropriate numerical optimization methods, such as the penalty function method. NC-DCMP is similar to the DCMP with diagonal loading (Li et al. 2003), which is also a stabilized version of DCMP. A significant advantage of using NC-DCMP is that it enables us to limit the maximal degradation of the shape of the main lobe without being affected by the strength of the incoming signal.

Ground clutters are removed by applying this algorithm to the observed data. Figure 5 shows a Doppler spectrum observed at Site A using clutter rejection. However, the atmospheric echo was also strongly suppressed because of an imperfect phase constraint due to mutual coupling and hiding of antennas, despite the greater stability of the NC-DCMP algorithm against such errors compared to DCMP.

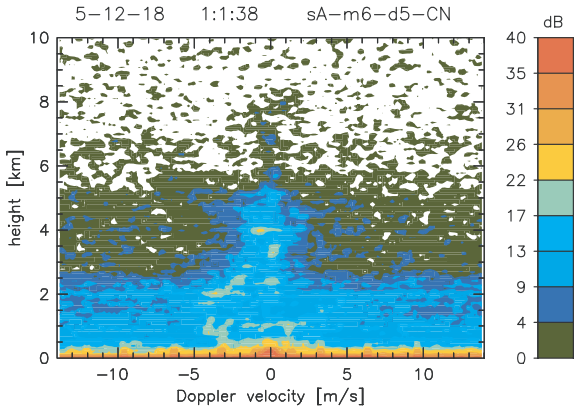

Fig. 5. Same as for Fig. 4, but with the adaptive clutter rejection.

5. Mutual coupling compensation

In a dense array, antennas are subject to electromagnetic coupling and hiding effects, which biases the phases in received signals. These effects impact not only the beam pattern but also, more severely, the robustness of the adaptive signal processing. In addition, the ground conditions, such as it being rough, smooth, wet, or dry, largely affect the signal phases. In practical observations, it is not easy to either measure or calculate all these effects quantitatively.

However, these effects can be estimated if the difference between the actual and expected phases, obtained from the geometrical configuration, is smooth in angular space. These effects are therefore measured using observed atmospheric echoes in a manner similar to that of the intrinsic phase measurement, with a small modification as

$$\psi_i = \boldsymbol{k}_i \cdot (\boldsymbol{r} - \boldsymbol{r}_0) + \varphi(\alpha, \beta)$$

where φ is an unknown function of direction cosines α and β, which are related to the zenith angle θ and azimuth ϕ with $\alpha = \sin\theta \sin\phi$ and $\beta = \sin\theta \cos\phi$. $\varphi(\theta, \phi)$ is the extended intrinsic phase function that includes the phase bias system caused by electromagnetic effects.

In order to represent the electromagnetic-inductive phase rotation system, φ is simply modeled as a linear function of the direction cosines as

$$\varphi_l(\alpha, \beta) = A\alpha + B\beta + C.$$

A, B, and C can then be estimated from a sufficient number of ψ_i measured from the brightest echoes in an observed data set. In the following discussion, we utilized bright echoes from 39 angular points for this purpose. To resolve the ambiguity of $\pm 2\pi N$ (N is an integer) in modeling the phase rotation as a function in the angular space, every phase value is set to fall within $\pm\pi$ from the

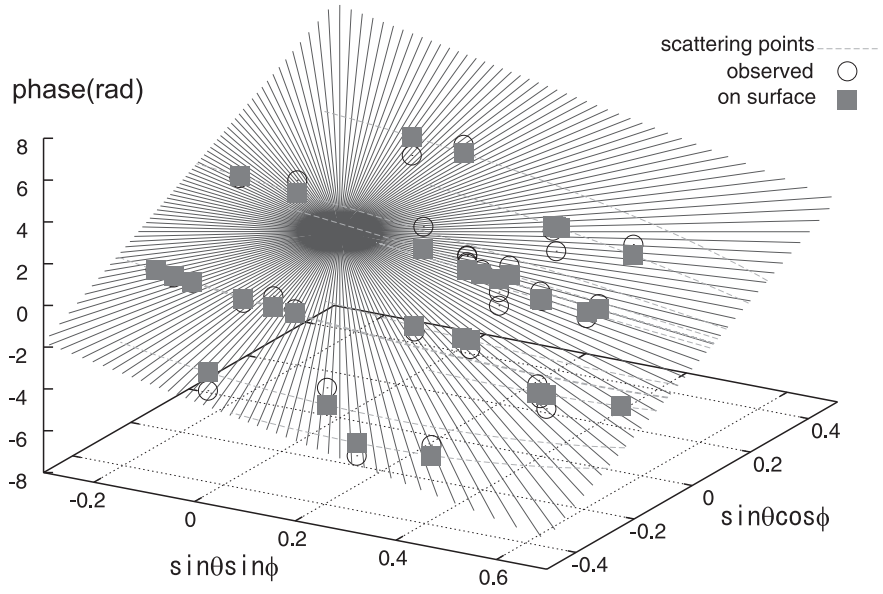

Fig. 6. Fitted linear function and the measured phase for observed data (open circles) of antenna no. 4 at Site A. Closed squares are the points on the surface of each corresponding open circle to show the residual difference. Lines indicate the passage of the scattering center viewed from the site.

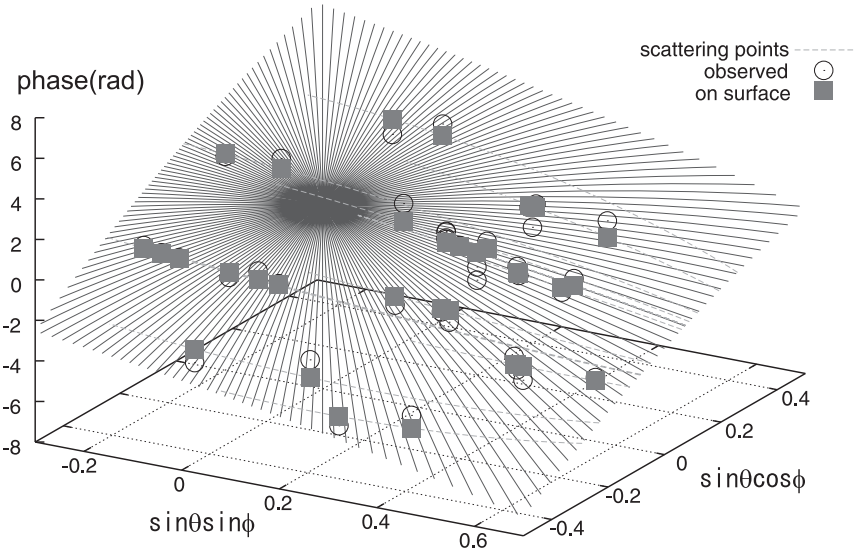

Fig. 7. Same as Fig. 6, but assuming a quadratic function instead of the linear function. Note that the fitted phase function is almost linear despite the increase in degrees of freedom.

adjacent direction (closest point measured with $\sqrt{(\alpha_1-\alpha_2)^2+(\beta_1-\beta_2)^2}$). Figure 6 shows a result for the fitted plane of the phase rotation system with antenna no. 4 at Site A.

Figure 8 shows a Doppler spectrum resulting from the estimated linear model $\varphi_l(\alpha,\beta)$. Ground clutters and the noise floor observed at the bottom of Fig. 4 were successfully removed. Specifically, a faint signal appeared above a height of 6 km, whereas it could be barely recognized in the spectrum by coherent synthesis.

To evaluate the goodness of the model, a quadratic function defined as

$$\varphi_q(\alpha,\beta)=A\alpha^2+B\beta^2+C\alpha\beta+D\alpha+E\beta+F$$

was also applied to the same data set. The fitted phase rotation function is illustrated in Fig. 7. In this figure, the estimated quadratic function looks almost linear, thereby implying that the first linear model should be sufficient. Figure 9 is the Doppler spectrum that resulted from the quadratic model. As the figure shows, the quadratic model is less stable than the linear model, especially at lower altitudes. This is because the phase bias system was estimated by fitting the brightest echoes, mostly from high altitude. Increasing the degrees of freedom causes the function to over-fit the given data set, and therefore, the adaptive process becomes

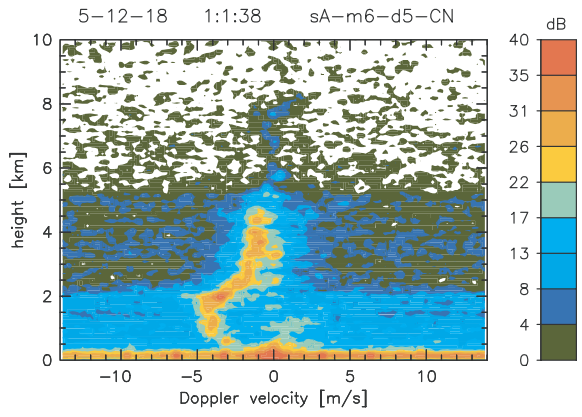

Fig. 8. Same as Fig. 5, but with the coupling compensation function $\varphi_l(\alpha,\beta)$.

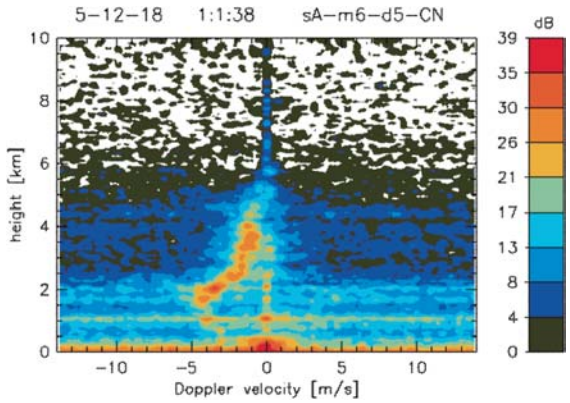

Fig. 9. Same as Fig. 8, but for $\varphi_q(\alpha,\beta)$.

Table 4. RMS residuals of the fitting of the phase error functions for each antenna. For antenna 1, the phase error is always 0.0 because the phase of antenna 1 is used as the standard.

	Linear Model		Quadratic Model	
No.	RMS (rad)	AIC	RMS (rad)	AIC
2	0.53	69.6698	0.52	73.4921
3	0.81	102.5210	0.80	107.0623
4	0.98	117.0890	0.92	118.0869
5	1.00	118.4064	0.96	121.4278
6	1.04	121.7183	0.95	120.4929
7	1.68	159.3234	1.61	161.6477
9	0.99	117.9147	0.91	117.5990
10	1.48	149.0068	1.26	142.9445
11	0.82	102.8513	0.81	108.2908
12	0.78	99.4241	0.76	103.3521
13	1.48	149.1805	1.33	146.9893

unstable at other altitudes despite a decrease in residual.

Table 4 shows root-mean-square (RMS) residuals of the fit and Akaike's information criterion (AIC; Akaike (1974)) for the two models applied to real data acquired at each antenna at Site A. As residuals of fitting must decrease by applying additional parameters if the data set is the same, the RMS residuals for the quadratic model are smaller than those for the linear model. However, a decrease observed for one data set does not immediately mean goodness of the model because an overfitted model works less accurately for another data set. Therefore, for evaluating multiple parametric models that have different degrees of freedom, a bias-compensated criterion should be employed. AIC is among the possible choices for evaluating the goodness of these parametric models. AIC values are presented in Table 4. As the model is better when AIC values are smaller, we chose the linear model for the following analyses.

6. Resulting three-dimensional wind field

6.1 An overview of the observed data

Using the proposed method, we processed the observed raw signal of 24 h, out of the 400 h observed in December 2005, and obtained a set of data of the wind field. Figure 13 presents the three-dimensional wind profile observed along Beam 1 during this period.

To see the spatial difference within the volume observed, Figs. 10 and 11 show the profiles of the horizontal components from 0600 to 1000 local

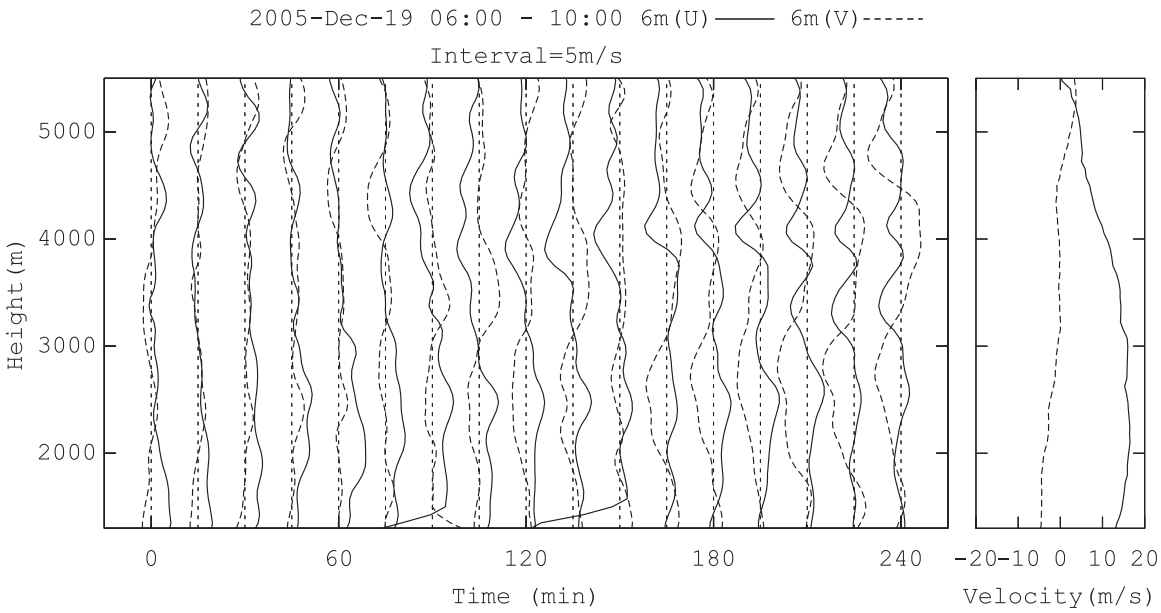

Fig. 10. Time variations of the profiles estimated with monostatic DBS averaged over 15 min each from 0600 to 1000 local time on December 19, 2005. The right small panel presents the time averages over the period, and the left larger panel shows the difference from the averages. The solid lines and the dashed lines correspond to the zonal and meridional components, respectively. The time interval of 15 min corresponds to the speed scale of 5 ms^{-1}.

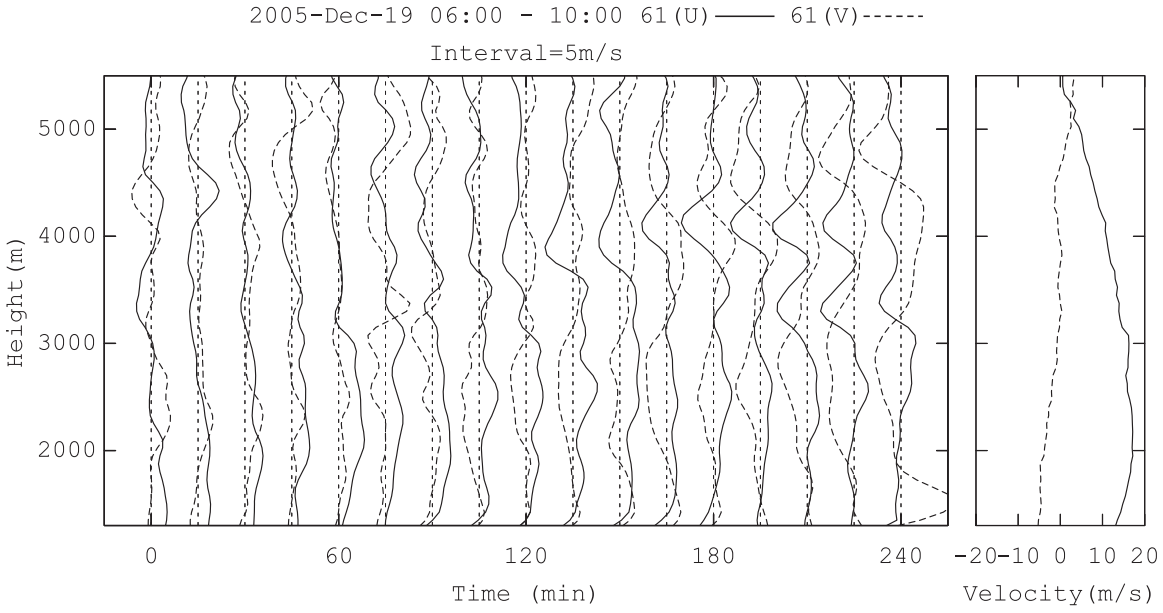

Fig. 11. Same as Fig. 10, but with the multistatic method.

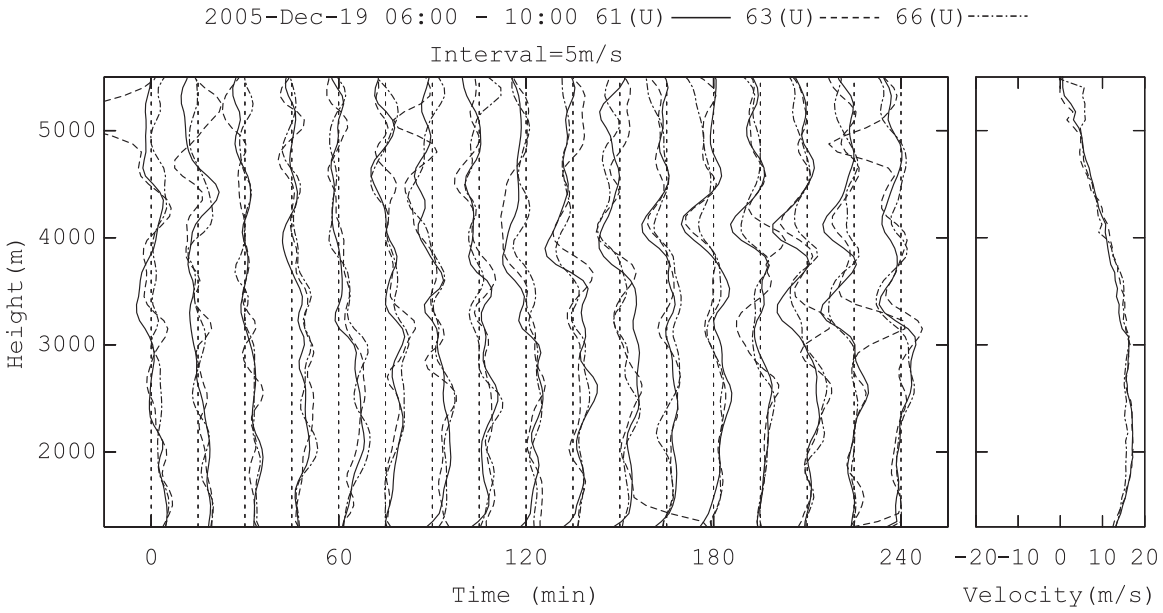

Fig. 12. Same as Fig. 11, but for the zonal wind profiles with Beam 1 (vertical, solid lines), 3 (eastward, dashed lines), and 6 (westward, dash-dot lines).

time (LT) in Fig. 13. The procedure used to draw the profiles is as follows. As for the two receiver sites, Doppler velocity was calculated at an interval of 75 m. Although the height resolution corresponding to the bandwidth of the transmitted pulses of EAR is 150 m, the receivers' output was at a rate of 0.5 μs and it was further resampled (interpolated) at every 75 m in height to align the spatial position of echoes. Estimated wind profiles were processed with a 3-point median filter followed by a convolution low-pass filter with coefficients [0.25, 0.5, and 0.25]. Hence, the overall

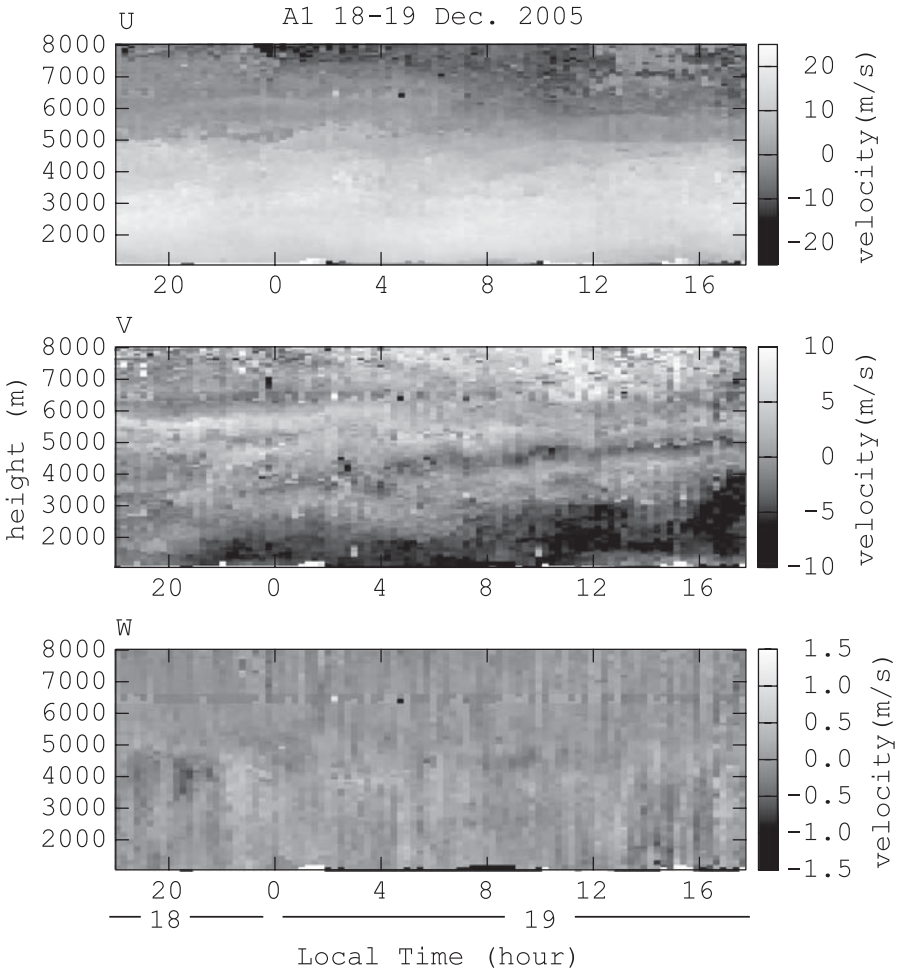

Fig. 13. Three-dimensional wind profiles at Beam 1 in Mode A (vertical) observed from 1800 on December 18 to 1800 on December 19, 2005.

height resolution in the final wind profiles was about 300 m. In each figure, the temporal average (right panels) and residual profiles (left panels) are plotted separately, and the velocity is scaled to meet 5 ms^{-1} with 15 min, which is equivalent to the time interval of the plots.

In Figs. 10 and 11, several wavy structures are seen, especially for the altitudes ranging from 3000 to 5000 m during this period. Comparing Figs. 10 and 11, the amplitude of the profiles obtained using the multistatic method is clearly larger than that using the monostatic DBS method. A direct comparison of both data sets is shown with scatter plots in Fig. 14. The line drawn in each panel shows the principal axis; the inclinations are 0.897 and 0.809 in the left and right panel, respectively. These inclinations are significantly lower than 1.0; this shows that, for a spatial fluctuation, the monostatic DBS provides a smaller estimate due to its averaging over a wider area than the multistatic method. Figure 14 also shows that the wind field is properly sampled and not too much over- or undersampled by the scanning beams. Therefore, the estimated horizontal scale of these fluctuations are much larger than the scanning beam width (about 1000 m).

The wind profiles estimated for Beam 1 along with Beams 3 and 6 with the multistatic system in this period are compared in Fig. 12. In this figure, vertical (solid lines), eastward (dashed lines), and westward (dash-dot lines) beams are presented. In the high fluctuation region from, which lies between 3000 and 5000 m, the three profiles show significant phase differences, especially after 105 min. These

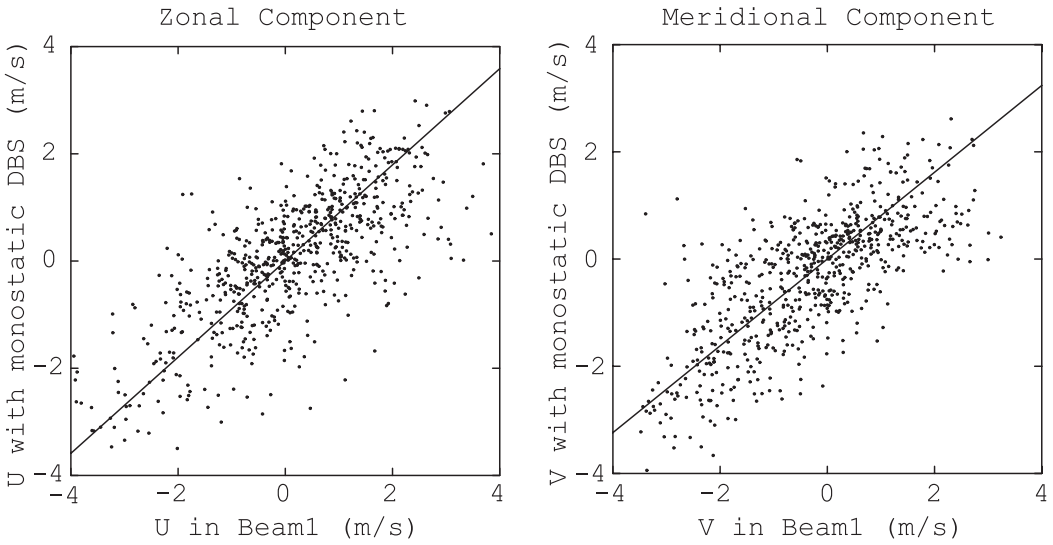

Fig. 14. Scatter plots of zonal (left) and meridional (right) components of the wind field observed with the multistatic method along the vertical beam (Beam 1) and with the monostatic DBS method using 4 off-vertical beams (Beams 2, 3, 5, and 6).

differences continued more than 15 min and are thought to be due to gravity waves.

Comparison of the wind profiles at 30 min also indicated that the vertical beam fluctuates almost out of phase to the other two and its amplitude is smaller. This should be due to the interference between multiple gravity waves. These profiles show the inclination of the waves and have information about their sources, though it is not yet achieved here.

6.2 *Analysis of spatial structure: a case study*

In order to induce a spatial structure of the wind field, the wind vectors are band pass filtered (instead of the 3-point low-pass filter described above) separately at each beam. This filter is a symmetric linear phase (non-dispersive) convolution FIR filter of the 14^{th} order with coefficients [−0.04908, −0.02376, −0.00005, −0.08128, −0.18278, −0.08652, 0.19973, 0.36269, 0.19973, −0.08652, −0.18278, −0.08128, −0.00005, −0.02376, and −0.04908]. The amplitude response of this filter is linearly plotted in the upper panel in Fig. 15. The "wavenumber" denotes the wavenumber per sample interval (dz = 75 m); a wavenumber of 0.5 corresponds to a wavelength of 150 m. Note that the scale of amplitude was not normalized and the response was carefully designed to reach 1.0 at its peak so that it did not magnify a small component more than what it really was. The lower panel of Fig. 15 shows the amplitude response of the filter as a function of wavelength. Lower and upper cutoff wavelengths (those at which the response crosses $\sqrt{2}/2 \sim 0.71$) can be roughly read as 300 and 1100 m, respectively. In the following part, all data are thus filtered.

Figure 16 shows hodographs of horizontal components along the 5 beams (from Beams 1 through 6, except for Beam 4) in Mode A on December 19, 0830. As shown above, the data are temporally averaged over 15 min. In each plot, the component is plotted from 3000, indicated with an open circle, to 3750 m at 75-m intervals.

Since the 4 off-vertical beams are tilted 10 degrees from the zenith, the horizontal spacing between Beam 1 (vertical) and the other beams is approximately 600 m. Although the horizontal scale is quite small and the data are averaged over 15 min, the hodographs are significantly different. Assuming that these differences are due to harmonic plane waves, we may analyze the components. Since this height region, the lower troposphere, is supposed to be a part of where gravity waves are generated, more than one harmonic wave should be assumed to analyze the spatial structure. We use a simple pseudo-inverse-based non-orthogonal decomposition analysis. First, the method is briefly explained for a superimposed 2-sinusoid case. Let $u(z_i)$ denote an observed data sequence as a function of height z_i. If u consists of

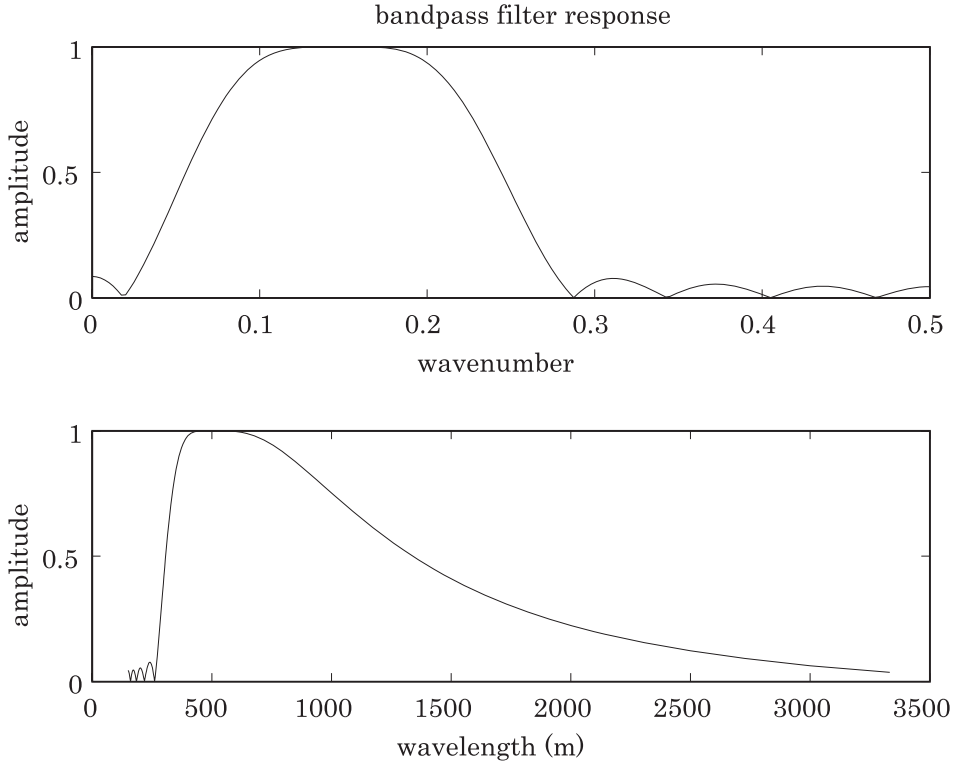

Fig. 15. The amplitude response of the bandpass filter plotted versus the wavenumber (top) and wavelength (bottom).

two sinusoids and random noise, it can be described as

$$u(z_i) = a_1 \sin(m_1 z_i + \phi_1) + a_2 \sin(m_2 z_i + \phi_2) + v(z_i). \quad (3)$$

In vector form, this is written as

$$\boldsymbol{u} = a_1 \boldsymbol{s}_1 + a_2 \boldsymbol{s}_2 + \boldsymbol{v} \quad (4)$$

where

$$\boldsymbol{u} = [u(z_1), \ldots, u(z_n)]' \quad (5)$$

$$\boldsymbol{s}_1 = [\sin(m_1 z_1 + \phi_1), \ldots, \sin(m_1 z_n + \phi_1)]' \quad (6)$$

$$\boldsymbol{s}_2 = [\sin(m_2 z_1 + \phi_2), \ldots, \sin(m_2 z_n + \phi_2)]' \quad (7)$$

and a_1, a_2, m_1, m_2, ϕ_1, and ϕ_2 are unknown. ($'$ denotes vector and matrix transposition.) Note that s_1 and s_2 are not generally orthogonal. Since one sinusoid with an initial phase is divided into sine and cosine components with two amplitude coefficients ($a_{\cdot s}$ and $a_{\cdot c}$ denote these coefficients multiplied with sine and cosine, respectively.), u is rewritten as

$$\boldsymbol{u} = B\boldsymbol{a} + \boldsymbol{n} \quad (8)$$

where

$$B = \begin{pmatrix} \sin m_1 z_1 & \cos m_1 z_1 & \sin m_2 z_1 & \cos m_2 z_1 \\ \vdots & \vdots & \vdots & \vdots \\ \sin m_1 z_n & \cos m_1 z_n & \sin m_2 z_n & \cos m_2 z_n \end{pmatrix} \quad (9)$$

$$\boldsymbol{a} = (a_{1s}, a_{1c}, a_{2s}, a_{2c}). \quad (10)$$

Note that the columns of B span a (four-dimensional, in this case) subspace (denoted by $\mathscr{S}$) identified with m_1 and m_2. Now, we obtain a least-square estimate $\tilde{\boldsymbol{a}}$ for $\boldsymbol{a}$ such that

$$\text{minimize } E^2 = \|\boldsymbol{u} - B\tilde{\boldsymbol{a}}\|^2. \quad (11)$$

According to fundamental linear algebra, the minimum is achieved when $B\tilde{\boldsymbol{a}}$ is the orthogonal projection of $\boldsymbol{a}$ to the subspace $\mathscr{S}$. Assuming $m_1 \neq m_2$, for simplicity, the necessary and sufficient condition for (11) is

$$B'\boldsymbol{u} = B'B\tilde{\boldsymbol{a}}. \quad (12)$$

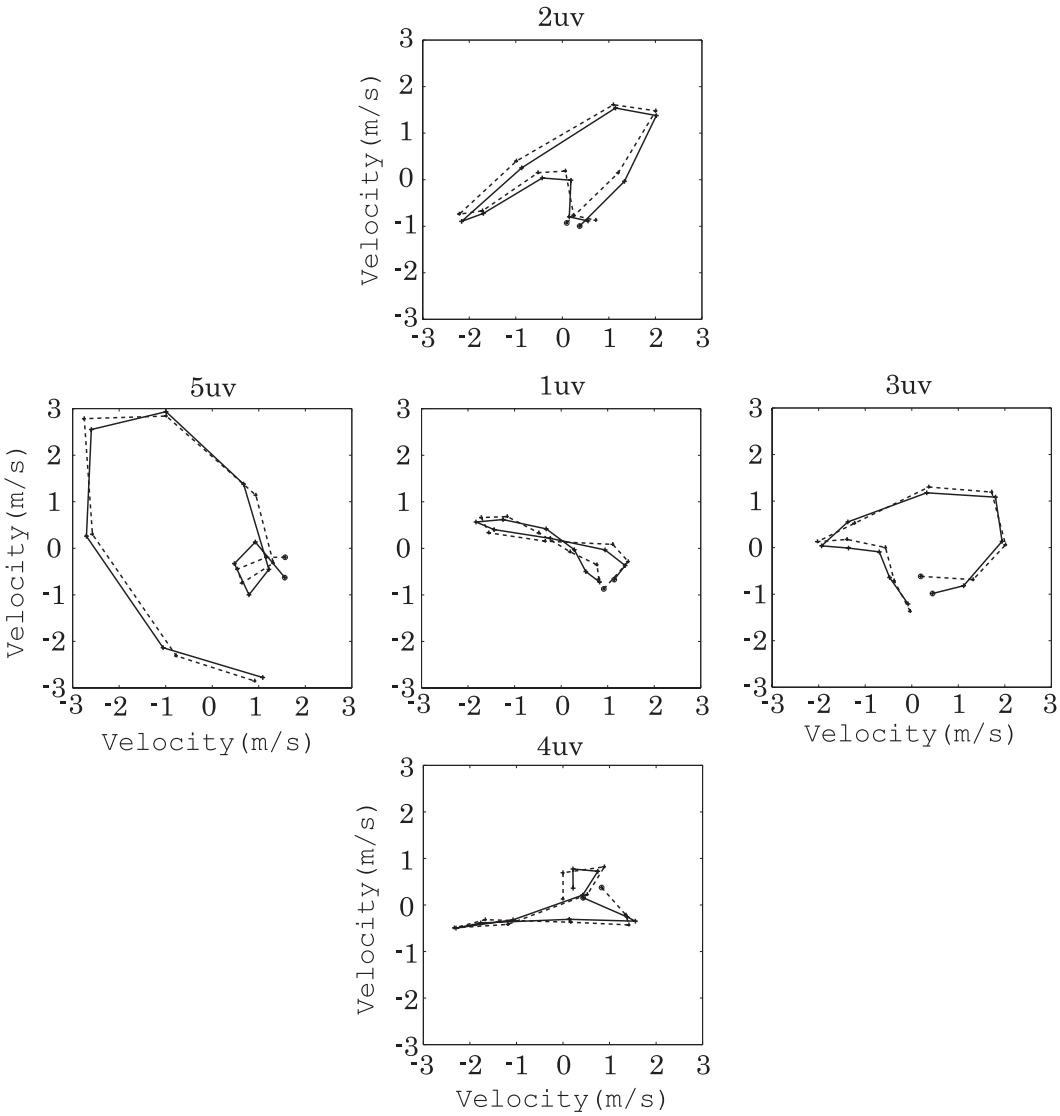

Fig. 16. (Dashed lines) Hodographs observed from 3000 to 3750 m in height along Beams 1 through 6 except for Beam 4. Lowest ($z = 3000$ m) point is marked with a circle and the height interval is 75 m. (Solid lines) Those fitted with two sinusoids (separately for each beam).

The solution is

$$\tilde{\boldsymbol{a}} = (B'B)^{-1}B'\boldsymbol{u}. \tag{13}$$

Then, E^2 is obtained from (11) as a function of m_1 and m_2. Finally, we can find the best solution by sweeping m_1 and m_2 within the wavenumber range allowed by the bandpass filter.

Figure 16 (solid lines) shows hodographs estimated with the method described above assuming two distinct superimposed sinusoids for each beam. This estimate was obtained by vectorizing (13); $\tilde{\boldsymbol{a}}$ and $\boldsymbol{u}$ are replaced with

$$A = \begin{pmatrix} a_{1us} & a_{1vs} \\ a_{1uc} & a_{1vc} \\ a_{2us} & a_{2vs} \\ a_{2us} & a_{2vc} \end{pmatrix} \quad \text{and} \quad U = \begin{pmatrix} u(1) & v(1) \\ \vdots & \vdots \\ u(n) & v(n) \end{pmatrix} \tag{14}$$

respectively. This result shows how simple addition of sinusoids can describe rather complex curves. Although the data is fit nicely, separate estimations for each beam do not properly provide the spatial

structure of the observed region. Therefore, we applied the least-square estimation to the data assuming multiple sinusoidal plane waves. This estimation was performed as follows. Since the sample points in the 3D space were not aligned in Cartesian grid points due to physical limitation of radar observation (sample points are conically aligned in Beams 2 through 6), it was impossible to divide the problem into three one-dimensional problems. Hence, we took a straightforward approach where observed data U and model B were additionally extended as

$$U = \begin{pmatrix} u_1(1) & v_1(1) \\ \vdots & \vdots \\ u_1(n) & v_1(n) \\ \vdots & \vdots \\ u_6(1) & v_6(1) \\ \vdots & \vdots \\ u_6(n) & v_6(n) \end{pmatrix} \tag{15}$$

and

$$B = \begin{pmatrix} \sin \boldsymbol{k}_1\boldsymbol{r}_1(1) & \cos \boldsymbol{k}_1\boldsymbol{r}_1(1) & \sin \boldsymbol{k}_2\boldsymbol{r}_1(1) & \cos \boldsymbol{k}_2\boldsymbol{r}_1(1) \\ \vdots & \vdots & \vdots & \vdots \\ \sin \boldsymbol{k}_1\boldsymbol{r}_1(n) & \cos \boldsymbol{k}_1\boldsymbol{r}_1(n) & \sin \boldsymbol{k}_2\boldsymbol{r}_1(n) & \cos \boldsymbol{k}_2\boldsymbol{r}_1(n) \\ \vdots & \vdots & \vdots & \vdots \\ \sin \boldsymbol{k}_1\boldsymbol{r}_6(1) & \cos \boldsymbol{k}_1\boldsymbol{r}_6(1) & \sin \boldsymbol{k}_2\boldsymbol{r}_6(1) & \cos \boldsymbol{k}_2\boldsymbol{r}_6(1) \\ \vdots & \vdots & \vdots & \vdots \\ \sin \boldsymbol{k}_1\boldsymbol{r}_6(n) & \cos \boldsymbol{k}_1\boldsymbol{r}_6(n) & \sin \boldsymbol{k}_2\boldsymbol{r}_6(n) & \cos \boldsymbol{k}_2\boldsymbol{r}_6(n) \end{pmatrix} \tag{16}$$

where u_i, v_i, $\boldsymbol{r}_i$, and $\boldsymbol{k}_j$ are zonal and meridional wind, three-dimensional position vector for the i^{th} beam ($i = 4$ is skipped) and wavelength vector for the j^{th} wave, respectively. For this estimation, we needed to scan multiple wavenumber vectors within the three-dimensional wavenumber space to find the best combination. As this process becomes difficult if the number of parameters becomes large, we decided to analyze in this part the structure of the field within the XZ cross section including Beams 1, 3, and 6.

Assuming that the structure consists of two plane waves, we obtained a result that did not fit the data sufficiently (not shown). Therefore, we assumed three plane waves to estimate the field structure. Figure 17 (upper row) shows the data at Beams 6, 1, and 3 (dashed lines) and the resulting fit (solid lines). These estimates did not fit the data as well as those obtained assuming two waves for each separate beam. However, these estimates describe the qualitative difference between the beams. Figure 17 (lower row) shows the estimated components. The estimated vertical and horizontal wave lengths ($\lambda = 2\pi/m_j$ and $\lambda_x = 2\pi/k_j$) were found to be, for $j = 1$ (solid lines), 2 (dot-dashed lines), and 3 (dashed lines), $\lambda_{z1} = 590$, $\lambda_{z2} = 770$, $\lambda_{z3} = 830$, $\lambda_{x1} = -480$, $\lambda_{x2} = -630$, $\lambda_{x3} = -670$, in meters.

If we assume that these waves are of topographic origin, some of the wave lengths estimated are shorter than the shortest limit at which a gravity wave can exist. This may imply that the observed region is not high enough to assume the existence of only a few sinusoidal plane waves because it should include more small components, including non-propagating ones, corresponding to the complexity of the topography. Hence, we do not deduce the physical structure of the wind field in term of this data set. Nevertheless, this result infers that the waves fitted to the wind field observed along one radar beam does not always describe the field structure when the surrounding data are considered. Further, the proposed method would work better in separating multiple components in a higher region, such as the stratosphere, in which more pure sinusoidal waves are expected.

7. Conclusions

In array beamforming, the accuracy of target pointing was decreased by mutual coupling between antennas, and this caused degradation of desired echo signals from the target atmosphere, especially when using an adaptive clutter rejection technique. To stabilize the effect, we propose a phase correction technique that uses the atmospheric echoes instead of calculating full electromagnetic effects between antennas and the ground, which includes a lot of unknown factors. This technique could be used because every single antenna had a sufficient SNR toward the atmospheric echo for determining the phase difference between echo signals received at separate receivers. To estimate the phase parameter to direct a beam to a point that was not included in reference targets, we applied a simple linear model to interpolate the 2D angular space. The validity of using the model was succinctly shown statistically using AIC.

In the previous section, we displayed data ob-

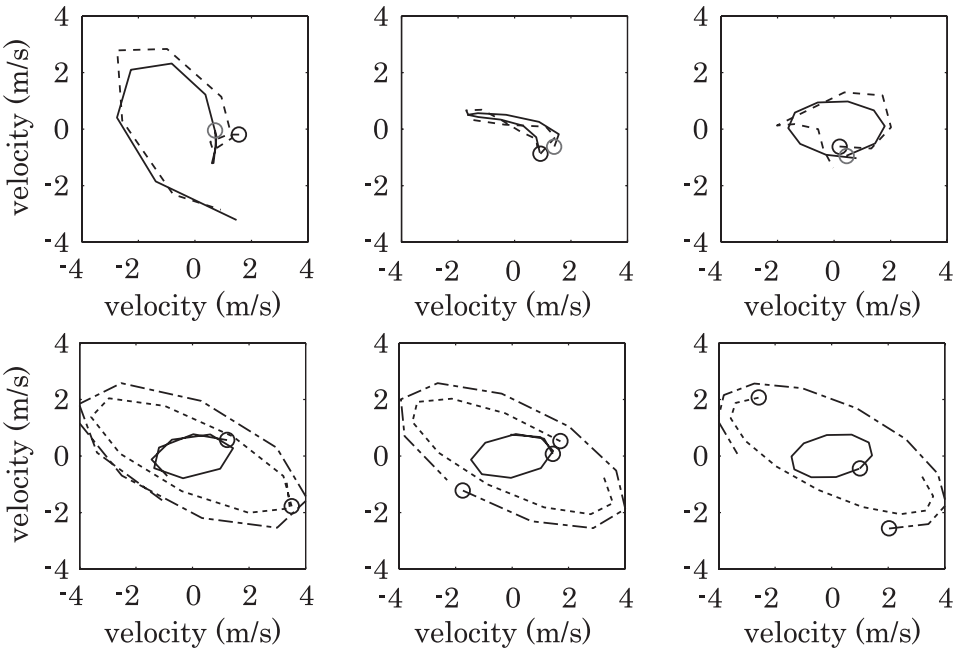

Fig. 17. Hodographs of the horizontal wind velocity of Beams 6 (left), 1 (center), and 3 (right). In the upper panels, dashed lines and solid lines show observed data (same as those in Fig. 16) and estimates assuming three sinusoidal plane waves, respectively. In the lower panels, each panel shows the corresponding three sinusoidal components.

tained using the proposed processes. Hodographs plotted in terms of horizontal wind velocity clearly showed spatial fluctuations of the wind field within a rather narrow region around the vertical beam. In order to analyze the field structure assuming multiple sinusoidal plane waves, we applied a least-square-based decomposition method using the linear generalized inverse. Assuming three such components, the field was approximately described, yet the residual was not insignificant. This may be because the plane wave model was too simple for the lower troposphere where many types of fluctuations are expected.

Acknowledgments

This study is supported by a Grant-in-Aid for Scientific Research (KAKENHI) on Priority Area-764 of the Ministry of Education, Culture, Sports, Science and Technology of Japan (Grant No. 13136205).

References

Akaike, H., 1974: A new look at the statistical model identification. *IEEE Trans. Autom. Contr.*, **AC-19**, 716–723.

Cox, H., R. M. Zeskind, and M. M. Owen, 1987: Robust adaptive beamforming. *IEEE Trans. Acoust., Speech, Signal Processing*, **ASSP-35**, 1365–1376.

Fukao, S., 2006: Coupling processes in the equatorial atmosphere (cpea): A project overview. *J. Meteor. Soc. Japan*, **84A**, 1–18.

Gal-Chen, T., and R. A. Kropfli, 1984: Buoyancy and pressure perturbations derived from dual-doppler radar observations of the planetary boundary layer: Applications for matching models with observations. *J. Atmos. Sci.*, **41 (20)**, 3007–3020.

Hudson, J. E., 1981: *Adaptive Array Principles*. Peter Perigrinus, London, UK.

Kamio, K., K. Nishimura, and T. Sato, 2004: Adaptive sidelobe control for clutter rejection of atmospheric radars. *Ann. Geophys.*, **22**, 4005–4012.

Li, J., P. Stoica, and Z. Wang, 2003: On robust capon beamforming and diagonal loading. *IEEE Trans. Signal Processing*, **51 (7)**, 1702–1715.

Nishimura, K., E. Gotoh, and T. Sato, 2006: Fine scale 3d wind field observation with a multistatic equatorial atmosphere radar. *J. Meteor. Soc. Japan*, **84A**, 227–238.

Ray, P. S., R. J. Doviak, G. B. Walker, D. Sirmans, J. Carter, and B. Bumgarner, 1975: Dual-doppler observation of a tornadic storm. *J. Appl. Meteor.*, **14**, 1521–1530.

Spano, E., and O. Ghebrebrhan, 1996: Sequences of complementary codes for the optimum decoding of truncated ranges and high sidelobe suppression factors for st/mst radar systems. *IEEE Trans. Geosci. Remote Sens.*, **34 (2)**, 330–345.

Stoica, P., Z. Wang, and J. Li, 2003: Robust capon beamforming. *IEEE Signal Processing Lett.*, **10**, 172–175.

Takao, K., M. Fujita, and T. Nishi, 1976: An adaptive antenna array under directional constraint. *IEEE Trans. Antennas, Propagat.*, **AP-24 (5)**, 662–669.

Wang, Z., J. Li, and P. Stoica, 2003: Comparison between norm constrained robust capon beamformers. *Proc. Phased Array Systems & Technology, IEEE Int. Symp.*, 170–175.

Ward, J., H. Cox, and S. M. Kogon, 2003: A comparison of robust adaptive beamforming algorithms. *Proc. Signals, Systems & Comp., IEEE Asilomar Conf.*, 1340–1344.

Wurman, J., S. Heckman, and D. Boccippio, 1993: A bistatic multiple-doppler radar network. *J. Appl. Meteor.*, **32**, 1802–1814.

Yamamoto, M., M. Fujiwara, T. Horinouchi, H. Hashiguchi, and S. Fukao, 2003: Kelvin-helmholtz instability around the tropical tropopause observed with the equatorial atmosphere radar. *Geophys. Res. Lett.*, **30 (9)**, 29–1.